Research Article

Nano Biomed Eng

The Novel MoS_2/MnO_2–BSA Nanocomposite Significantly Enhances Antitumour Efficacy through Synergistic Photothermal Therapy/Hemodynamic Therapy

Lingle Zhang[1,§], Xiaoqing Qian[2,3,§], Yingying Yang[1], Tingting Xiang[4], Jinrong SiTu[1], Hongzhang Yan[1], Kai Yang[1,5,6]✉

[1] College of Fisheries and Life Science of Shanghai Ocean University, Shanghai 201306, China
[2] Institute of Nano Biomedicine and Engineering, Shanghai Engineering Research Centre for Intelligent Diagnosis and Treatment Instruments, Department of Instrument Science and Engineering, School of Electronic Information and Electrical Engineering, Shanghai Jiao Tong University, Shanghai 200240, China
[3] National Engineering Research Center for Nanotechnology, Shanghai 200241, China
[4] School of Clinical Laboratory Science, Guizhou Medical University, Guiyang 550004, China
[5] Department of Imaging Medicine and Nuclear Medicine Tongji Hospital, Shanghai 200065, China
[6] Shanghai Jiao Tong University Affiliated Sixth People's Hospital, Shanghai 200233 China

[§] These authors contributed equally to this work.

✉ Corresponding author. E-mail: 2305080@tongji.edu.cn

Received: May 16, 2024; **Revised:** Jun. 3, 2024; **Accepted:** Jul. 10, 2024

Citation: L.L. Zhang, X.Q. Qian, Y.Y. Yang, et al. The novel MoS_2/MnO_2–BSA nanocomposite significantly enhances antitumour efficacy throughsynergistic photothermal therapy/hemodynamic therapy. *Nano Biomedicine and Engineering*, 2025, 17(2): 277−286.
http://doi.org/10.26599/NBE.2024.9290105

Abstract

Cellular photothermal and chemical kinetic therapy has recently been acknowledged as an effective cancer treatment method. Photothermal therapy (PTT) works by transforming light energy into heat through the photothermal effects triggered by near-infrared (NIR) laser exposure. The employment of nanomaterials as carriers for PTT agents or as PTT agents themselves offers improved therapeutic outcomes with fewer side effects through enhanced photothermal conversion efficiency, accumulation of the PTT agents in the tumor tissue. In this work, we synthesized new MoS_2/MnO_2 nanomaterials modified with bovine serum protein to enhance the effectiveness of the Fenton-like reaction between MoS_2 and MnO_2 to produce •OH through photothermolysis excitation using a near-infrared (NIR) 808 nm laser. *In vitro* measurements further confirmed the exceptional ability of MoS_2/MnO_2–modified bovine hemoglobin (BSA) to destroy cancer cells. We believe that photothermal therapy can offer new insights into cancer therapy and greatly enhance the efficacy of chemotherapeutic tumor treatments.

Keywords: nanomaterials; photothermal therapy; chemical kinetics; synergistic therapy

Introduction

Currently, cancer is the leading cause of death worldwide. The principal tumor can be removed by standard surgery, radiation therapy, or chemotherapy. However, this malignancy is extremely difficult to cure because of metastases, and serious adverse effects can occur. Chemodynamic therapy (CDT)

based on Fenton and Fenton-like reactions has garnered increasing attention recently due to its ability to produce highly toxic •OH in the tumor lesion area with few side effects and high specificity. Hydrogen peroxide (H_2O_2) produces highly oxidized hydroxyl radicals, which can be produced by ferrous or nonferrous metal ions, to eliminate organic pollutants. This process is known as CDT [1–5].

The mild acidity, severe hypoxia, and overexpression of H_2O_2 in the tumor microenvironment (TME) facilitate tumor growth and metastasis [6]. Thus, creating nanoplatforms to treat tumors using the TME appears promising. CDT, which generates harmful •OH catalyzed by metal ions (e.g., Fe, Mn, Co, Ag, and Cu), is thought to be an effective cancer treatment based on cytoplasmic H_2O_2 [7–16]. Because of their high •OH production and safety, manganese dioxide nanoparticles are among the most commonly employed in the TME. However, obtaining an anticipated therapeutic effect with CDT alone is challenging because of the low H_2O_2 concentration in the TME.

Due to its minimal cost and few side effects, photothermal treatment (PTT) has garnered significant attention globally. Photothermal agents (PTAs) can promote tumor cell necrosis by converting light into heat when exposed to near-infrared (NIR) radiation. Concurrently, the heat produced by the PTAs can effectively boost the manufacturing efficiency of •OH [17–19].

Two-dimensional (2D) molybdenum disulfide (MoS_2) nanosheets are used because of their high photothermal conversion efficiency and notable NIR absorbance [20–22]. MoS_2 nanosheets can catalyze the breakdown of H_2O_2 to produce •OH by mimicking peroxidise [2,17,23]. Glutathione and the MnO_2 shell can have a redox reaction to form glutathione disulfide and Mn^{2+}. Interestingly, bicarbonate (HCO_3^-) must be present for the Fenton-like reaction to be driven by Mn^{2+}. Notably, HCO_3^-/CO_2, one of the most significant physiological buffers, may supply enough HCO_3^- to sustain the Mn^{2+}-induced •OH production from H_2O_2. Therefore, by acting as cocatalysts and having a synergistic photothermal impact, MoS_2 nanosheets are a promising option to improve the CDT's treatment efficacy.

In this research, innovative MoS_2/MnO_2–modified bovine hemoglobin (BSA) nanocomposites were designed and produced based on these concepts. In •OH production, MoS_2/MnO_2–BSA was more effective than MnO_2 or MoS_2 alone, indicating that the catalytic approach can increase the effectiveness of the Fenton-like reaction. Furthermore, because of MoS_2's capacity to absorb light at 808 nm, the photothermal effect caused by MoS_2/MnO_2–BSA with an 808 nm NIR laser was utilized for the first time to further increase the efficiency of •OH synthesis. The findings indicated high therapeutic efficacy *in vitro*. They demonstrated that PTT and CDT effectively killed cancer cells *in vivo* when combined. As a result, this work suggests a cooperative approach that combines catalysis with the NIR laser-excited photothermal effect to create highly effective and minimally harmful nanotherapeutic medications [14–27].

Materials and Methods

Materials

Ammonium molybdate, thiourea, N-acetyl cysteine (NAC), iron(III) acetylacetonate (99.9%), trioctylamine (98%), oleic acid (90%), nitrosodiammonium tetrafluoroborate ($NOBF_4$), BSA, terephthalic acid (PTA) (99%), $(NH_4)_2MoS_4$, hydrazine hydrate (N_2H_4, 85%), and PAH (M_W = 17 500) were purchased from Aladdin Biochemistry Science and Technology Co. (Shanghai, China). Potassium permanganate ($KMnO_4$, 99%) was provided by China National Pharmaceutical Chemical Reagent Co. (Shanghai, China). Phosphate buffer saline (PBS) (pH 6.0) and deionized water were used throughout the experiments.

Propidium iodide (PI), calcein acetoxymethyl (Calcein AM), and 2,7-dichlorofluorescein diacetate (2,7-dichlorofluorescein) were obtained from Sigma Aldrich (MO, USA). The CCK-8 assay was provided by Dalian Meilun Biotechnology Co. (Dalian, China).

MoS_2/MnO_2–BSA nanomaterial production

MoS_2 nanosheet preparation

$(NH_4)_2MoS_4$ was used as a precursor in a single-step hydrothermal process to create MoS_2 nanosheets. $(NH_4)_2MoS_4$ was typically dissolved in 50 mL of water. After 10 min of sonication, N_2H_4 was introduced as a reducing agent. Subsequently, the mixture was incubated for 6 h at 180 °C in a brushed stainless steel boiler lined with 100-mL Teflon. Anhydrous ethanol was used to wash the MoS_2

nanosheets three times after they had naturally cooled to room temperature.

Preparation of MoS_2/MnO_2 nanoparticles

10 mL of deionized water was mixed with 1 mL of MoS_2 nanosheets (1 mg·mL^{-1}) and 10 mL of $KMnO_4$ (10 mg·mL^{-1}) before being supplemented with 50 mL of PAH (23.6 mg·mL^{-1}). The liquid quickly turned from purple to brown after PAH was added. The mixed solution was centrifuged for 30 min at 13 000× *g* after the reaction to obtain MoS_2/MnO_2 nanoparticles. The residue was then cleaned 3 times with anhydrous ethanol and resuspended in 1 mL of deionized water.

Preparation of MoS_2/MnO_2–BSA nanoparticles

The MoS_2/MnO_2 solution was mixed with 10 mL of ionized water and moderately agitated at room temperature (~ 1 000 r·min^{-1}) to form MoS_2/MnO_2–BSA nanoparticles. BSA was added dropwise, and the solution was stirred overnight. After centrifugation at 13 000× *g* for 30 min, the mixed solution was rinsed three times with deionized water and reconstituted in 1 mL.

Nanoparticle characterization

TEM (JEM-2100F, Japan) was used to assess the nanoparticle size and morphology. The nanoparticles were subjected to dynamic light scattering measurements and zeta potential analysis utilizing a Nicomp 380 ZLS zeta potential/particle size meter (Nicomp 380, USA). A Varian Cary 50 spectrophotometer (Varian Inc., Palo Alto, CA, USA) and an infrared thermal camera (FLIR T420, Fluke, USA) recorded the ultraviolet (UV)–visible (Vis) absorption spectra. PTA was detected with a fluorescence spectrometer (F-4800).

PT conversion efficiency of MoS_2/MnO_2–BSA

The MoS_2/MnO_2–BSA nanomaterial solution (300 μg·mL^{-1}) was subjected to an 808 nm light for 10 min at a laser power of 1.0 W·cm^{-2}. Then, the solution was cooled naturally for 10 min. A thermocouple probe detected the temperature change every minute. In earlier research, the PT conversion efficiency was computed. A 300 μg·mL^{-1} MoS_2/MnO_2–BSA nanomaterial combination was exposed to 10 and 60 min of 808 nm laser (1.0 W·cm^{-2}) radiation in tube centrifuges to ensure thermal stability.

$$\eta = \frac{hs(T_{max} - T_{surr}) - Q_{dis}}{I(1 - 10^{-A_{sos}})}$$

where h and s are the heat transfer coefficient and the sample container surface area, respectively. T_{surr} is the ambient temperature, T_{max} is the resultant maximum temperature, η is the PT conversion efficiency, Q_{dis} represents the heat loss, A is the MoS_2/MnO_2–BSA solution's absorbance at 808 nm, and I is the incident laser power.

$$\tau_s = \frac{m_D C_D}{hs}$$

where C_D is the heat capacity (4.2 × 10^3 J/(kg·°C)), m_D is the solvent mass (0.3 g), and τ_s is the time constant of the specimen system. Finally, the MoS_2/MnO_2–BSA PT conversion rate was determined to be 21.8%.

Extracellular •OH detection

2 mL of a PBS mixture (pH 6.0) containing H_2O_2 (8 mmol/L) and PTA as a dye probe (25 mg·L^{-1}) was used, and the level of fluorescence was measured over time (EX: 315 nm, EM: 425 nm).

The following sample solutions were used: MoS_2 nanosheets + 8 mmol·L^{-1} H_2O_2, 8 mmol·L^{-1} H_2O_2 + 0.5 mmol·L^{-1} $MnCl_2$ + 25 mmol·L^{-1} $NaHCO_3$ buffer solution, and MoS_2 nanosheets + 8 mmol·L^{-1} H_2O_2 + 0.5 mmol·L^{-1} $MnCl_2$ + 25 mmol·L^{-1} $NaHCO_3$ buffer solution.

•OH production was measured at various H_2O_2 concentrations. Buffer solutions of MoS_2 nanosheets + 8 mmol·L^{-1} H_2O_2 + 0.5 mmol·L^{-1} $MnCl_2$ + 25 mmol·L^{-1} $NaHCO_3$ were made with varying H_2O_2 quantities (0, 1, 2, 8, and 16 mmol·L^{-1}). TA was added to the solution, and its fluorescence was measured by spectroscopy at 430 nm.

•OH generation was measured within a range of pH values. Solutions of MoS_2 nanosheets + 8 mmol·L^{-1} H_2O_2 + 0.5 mmol·L^{-1} $MnCl_2$ + 25 mmol·L^{-1} $NaHCO_3$ acetate buffer (pH 7.4, 6.5, and 5.0) were used. •OH-induced light amplification was monitored, measuring the fluorescence level at 430 nm.

•OH generation was also measured at various temperatures. The sample solution comprised MoS_2 nanosheets + 8 mmol·L^{-1} H_2O_2 + 0.5 mmol·L^{-1} $MnCl_2$ + 25 mmol·L^{-1} $NaHCO_3$. The mixture was heated to room temperature (RT), 37 °C, and 50 °C for 10 min. The fluorescence intensity at 430 nm was used to track the •OH-induced fluorescence.

Photothermal effect of the MoS_2/MnO_2–BSA nanocomposites

After 10 min of 808 nm laser irradiation (1.0 W·cm^{-2}), the temperature of the MoS_2/MnO_2–BSA nanocomposite solution (with a mass concentration of 300 μg·mL^{-1}) was recorded at 1 min intervals using a thermocouple probe. The temperature variations were captured using an infrared thermographic camera to determine the solution's thermal stability.

Cell experiments

Cell culture

Gastric cancer cells (MGC-803) were cultured on high-sugar DMEM at 37 °C and 5%CO_2.

Cellular uptake analysis

MGC-803 cells were inoculated into 12-well plates (1×10^4 cells per well) and treated with MoS_2/MnO_2–BSA–rhodamine B (RhB) for 0, 1, 2, and 6 h using a flow cytometer and FlowJo software 10.8.1. Stained cells were then examined.

Cytotoxicity determination of MoS_2/MnO_2–BSA nanomaterials

MGC-803 cells were injected overnight at 37 °C and 5%CO_2 in 96-well plates. MoS_2/MnO_2–BSA nanocomposites at 0, 50, 100, 300, and 500 μg·mL^{-1} were added, and cells were incubated for a full day. MGC-803 cells were subjected to two PBS washes. Subsequently, 100 μL of the CCK-8 solution was added, and cells were incubated for 1 h. The 96-well plates were subsequently examined in a plate reader to determine cell viability, and their absorbance was measured at 450 nm. In addition to including H_2O_2, which was utilized to mimic the cytotoxicity of MoS_2/MnO_2–BSA nanomaterials in the TME, the experiments were identical to those described above.

In vitro photothermal promotion of CDT by MoS_2/MnO_2-BSA nanomaterials

MGC-803 cells were injected overnight at 37 °C and 5%CO_2 in 96-well plates. Next, HeLa cells containing H_2O_2 (0.02 mmol·L^{-1}) were treated with MoS_2/MnO_2–BSA nanosolutions (0, 50, 100, 300, and 500 μg·mL^{-1}) for 24 h. The cells were subjected to 10 min of 808 nm laser (1.0 W·cm^{-2}) irradiation, followed by two PBS washes and 1 h of incubation with 100 μL of CCK-8. The plates were then examined with a plate reader to determine cell viability, and their absorbance was measured at 450 nm.

In vitro reactive oxygen species generation

H_2O_2-filled 6-well plates were inoculated with MGC-803 cells for 12 h. MoS_2/MnO_2–BSA (300 μg·mL^{-1}) was added, and the combination was incubated for 4 h. Following a 5 min incubation with DCFH-DA (10 μmol·L^{-1}) with or without 808 nm laser irradiation (1.0 W·cm^{-2}), the cells were rinsed twice with PBS before fluorescence microscopy.

Apoptosis analysis

The cytotoxic effect of MoS_2/MnO_2–BSA was examined using the Membrane-Associated Protein V-FITC/PI Apoptosis Detection Kit. MGC-803 cells were cultivated overnight in 24-well plates with 1×10^5 cells per well. After incubation for 12 h, the medium was replaced with a fresh medium containing MoS_2/MnO_2–BSA. The solution was then removed, exposing the cells to laser irradiation. FITC and PI were subsequently applied following the manufacturer's guidelines. The stained cells were examined by flow cytometry, and FlowJo software 7.6.1 was used to evaluate the data.

In vitro therapeutic effect of MoS_2/MnO_2–BSA

MGC-803 cells were grown in six-well plates for 12 h. After adding 300 μg·mL^{-1} MoS_2/MnO_2–BSA and DMEM (containing H_2O_2), the mixture was incubated for 4 h. Then, the cells were exposed to an 808 nm laser (1.0 W·cm^{-2}) for 10 min on each side. Cells were then washed twice with PBS and exposed to calcein AM and PI for 30 min. The cell morphology of the samples was observed by fluorescence microscopy after two PBS washes.

Results and Discussion

Preparation and characterization

MoS_2 nanosheets with a median size of 100 nm were created (Fig. 1(a)), indicating the superior distribution and size homogeneity of the fabricated materials. The combined precipitation approach was utilized to generate MoS_2/MnO_2 complexes. The cationic polyelectrolyte PAH was used as a reducing agent to convert $KMnO_4$ on the surface of MoS_2 particles to MnO_2. The MoS_2/MnO_2 molecules were also washed using anhydrous ethanol, and sedimentation was performed to eliminate excess impurities.

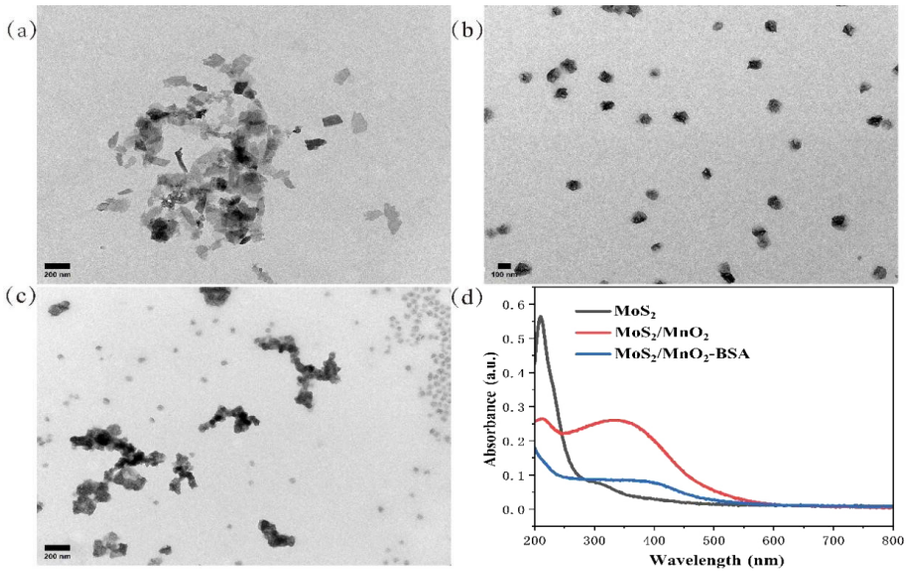

Fig. 1 Characterization of the MoS_2/MnO_2–BSA nanocomposites. **(a)** TEM images of the MoS_2 nanosheets. **(b)** TEM images of the MoS_2/MnO_2 nanomaterial. **(c)** TEM images of the MoS_2/MnO_2–BSA nanomaterial. **(d)** UV–Vis penetration spectra of MoS_2, MoS_2/MnO_2, and MoS_2/MnO_2–BSA.

Figure 1(b) illustrates the efficient encapsulation of rosette-like MnO_2 outside the MoS_2 nanosheets. The color consumption of the MnO_2-wrapped MoS_2 nanosheets changed significantly, as indicated by the UV absorption diagram (Fig. 1(d)), because MnO_2 had an absorption peak at 300–400 nm. The MoS_2/MnO_2 nanocomposites were then produced by electricity and modified with bovine serum albumin (BSA) to increase their biological compatibility (Fig. 1(c)).

The final produced nanomaterials contained a positive charge, as indicated by the charge measurements we took of the nanomaterials in aqueous solution at each stage (Fig. 2(a)). Because strongly charged nanoparticles are easily dissolved in water, their blood circulation period is prolonged. Furthermore, MoS_2/MnO_2–BSA, with a size of 236 nm, enters the tumor more easily and readily accumulates there (Fig. 2(b)).

PT effect of MoS_2/MnO_2–BSA

We examined the MoS_2/MnO_2–BSA nanoparticles' penetration strength at 808 nm, which demonstrated the MoS_2 nanomaterials' good photothermal capabilities. The mercury in the MoS_2/MnO_2–BSA solution increased from 26 to 51.8 °C at 300 μg·mL^{-1} and a laser power density of 1.0 W·cm^{-2}. In contrast, the temperature of the water increased by less than 4 °C (Fig. 3(a)). The MoS_2/MnO_2–BSA nanocomposite had a PT conversion efficiency of 21.8% (Fig. 3(d)). After three cycles of laser irradiation, the temperature of the MoS_2/MnO_2–BSA solution did not significantly decrease, indicating that MoS_2/MnO_2–BSA has good PT stability (Fig. 3(c)). These findings suggest that MoS_2/MnO_2–BSA nanoparticles have a wide range of possible uses [28].

Reactive oxygen species generation by MoS_2/MnO_2–BSA

PTA was chosen as a fluorescent probe to track •OH generation in PBS at pH 6.0 to evaluate the •OH generation capacity of the MoS_2/MnO_2–BSA nanocomposites. Its fluorescence absorption at 425 nm increased with increasing •OH. The •OH production capacity of MoS_2/MnO_2–BSA was greater than that of MnO_2 and MoS_2 alone and more significant than that of their combined amount (MnO_2 + MoS_2) (Fig. 2(c)). This result suggests that treating MoS_2 and MnO_2 synergistically may increase the efficiency of •OH production. The fluorescence intensity of PTA increased with increasing H_2O_2 concentration and solution acidity (Figs. 2(d) and 2(e)). Most notably, when the temperature increased, the PTA fluorescence intensity increased noticeably. This result was due to the ionization process intensifying at high temperatures (Fig. 2(f)). These results support the application of MoS_2/MnO_2 nanocomposites for PT-enhanced CDT.

Cytotoxicity assay of MoS_2/MnO_2–BSA nanoparticles

Before administering MoS_2/MnO_2–BSA to the cancer

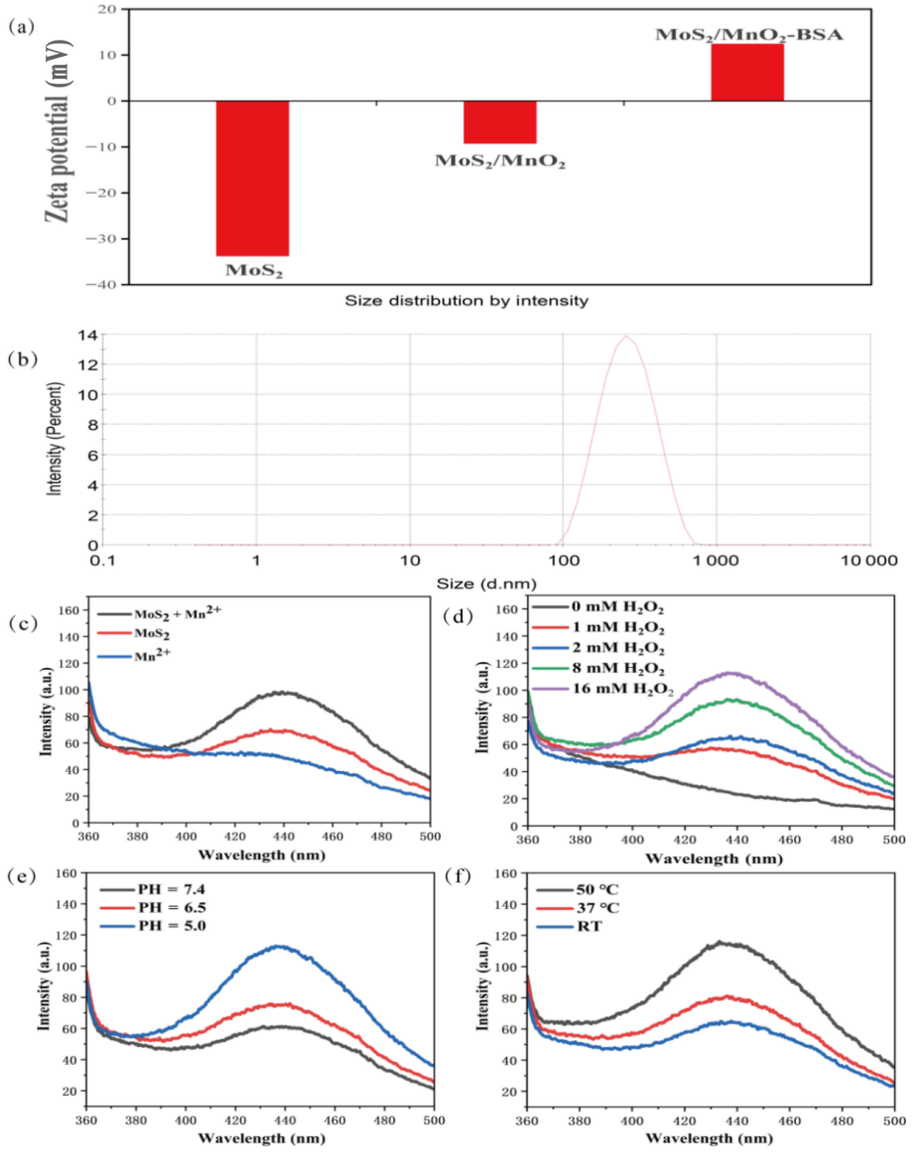

Fig. 2 (a) Potentials of MoS_2, MoS_2/MnO_2, and MoS_2/MnO_2–BSA. **(b)** Size analysis of MoS_2/MnO_2-BSA nanoparticles. **(c)** PTA-mediated Fenton-like reactions in multiple solutions. **(d)** •OH generation at various H_2O_2 values. **(e)** •OH production at various pH levels. **(f)** •OH production at various temperatures.

cells, the molecular absorption behavior of the compound was studied. MoS_2/MnO_2–BSA was labeled with RhB, and MoS_2/MnO_2–BSA uptake increased with increasing fluorescence intensity over time (Fig. 3(g)).

Next, the biological compatibility of MoS_2/MnO_2–BSA was investigated. When MGC-803 cells were coincubated with varying doses of MoS_2/MnO_2–BSA, the percentage of surviving cells remained as high as 84%, suggesting that MoS_2/MnO_2–BSA has strong biocompatibility and low cytotoxicity (Fig. 3(e)). On the other hand, in the activated TME (200 μmol·L^{-1} H_2O_2), the cell viability decreased with increasing MoS_2/MnO_2–BSA nanocomposite concentration. This phenomenon may be related to •OH production-induced damage to the MGC-803 cells. After 10 min of 808 nm laser exposure, the Fenton reaction measured photothermal generation at approximately 55 °C (Fig. 3(a)), resulting in no more than 10% cell survival and demonstrating the practical antitumor efficacy of the combined PTT-enhanced CDT (Fig. 3(f)).

In vitro reactive oxygen species generation

2,7-Dichlorofluorescein diacetate (DCFH-DA), a glowing probe, was used to monitor the generation of reactive oxygen species (ROS) to confirm that reactive •OH was produced in the cells. ROS exhibited green fluorescence when activated by •OH. Figure 4 illustrates the mild green emission observed following treatment with the MoS_2/MnO_2–BSA

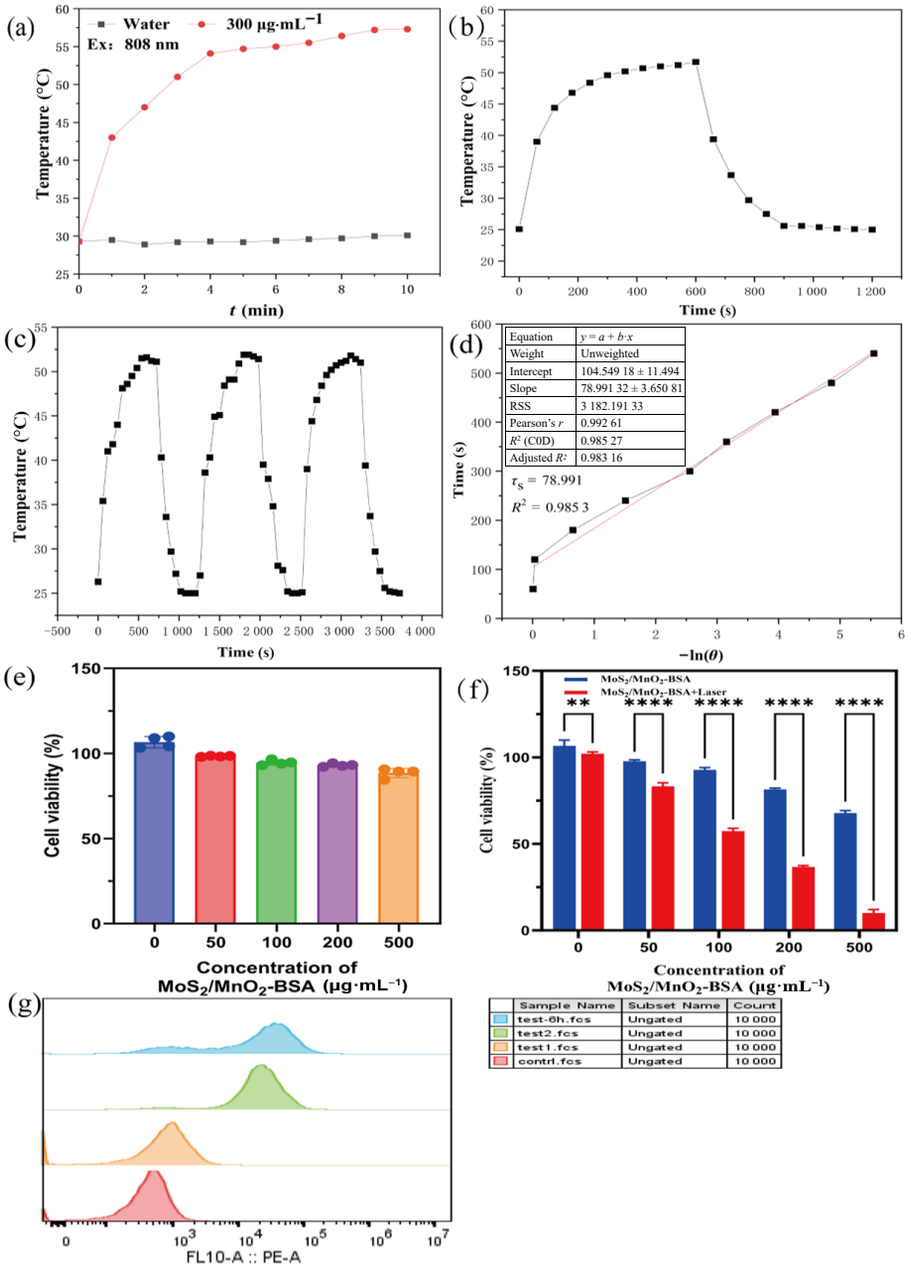

Fig. 3 (a) Curve of MoS_2/MnO_2–BSA (300 μg·mL^{-1}) and water under NIR laser irradiation (808 nm, 1.0 W·cm^{-2}, 10 min). **(b, c)** Temperature gradients plotted against time for MoS_2/MnO_2–BSA nanomaterial solutions (300 μg·mL^{-1}) exposed to 808 nm laser radiation (1.0 W·cm^{-2}). **(d)** The linear fitting curve of nanomaterial cooling for 10 min (red line, τ_s = 78.991 s). **(e)** MGC-803 cell viability under various conditions (mean ± SD; N = 3); **(f)** MGC-803 cell viability under various MoS_2/MnO_2–BSA concentrations (mean ± SD; N = 3). **(g)** MoS_2/MnO_2–BSA–RhB-treated MGC-803 cells were subjected to flow cytometry at four different time points: 0, 1, 2, and 6 h.

nanocomposites compared to that of the laser and control groups (Figs. 4(a)–(b)). This observation suggests that the Fenton-like reaction between MoS_2/MnO_2 and H_2O_2 generates •OH in the MGC-803 cells. Furthermore, the MoS_2/MnO_2–BSA+ 808-nm laser group exhibited significantly increased green fluorescence (Fig. 4(d)), implying that the photothermal impact of MoS_2/MnO_2–BSA nanoparticles induced by NIR laser irradiation may substantially boost the •OH production rate [29].

Apoptosis analysis

Following laser irradiation, the PBS group cells exhibited the lowest necrosis and apoptosis levels, suggesting that the cells may withstand laser irradiation at the essential power density (Fig. 4(e)). In contrast, the MoS_2/MnO_2–BSA + laser group had significantly fewer cells, and most cells were late apoptotic. The MoS_2/MnO_2–BSA group had a minor inhibitory effect on the cells relative to the control

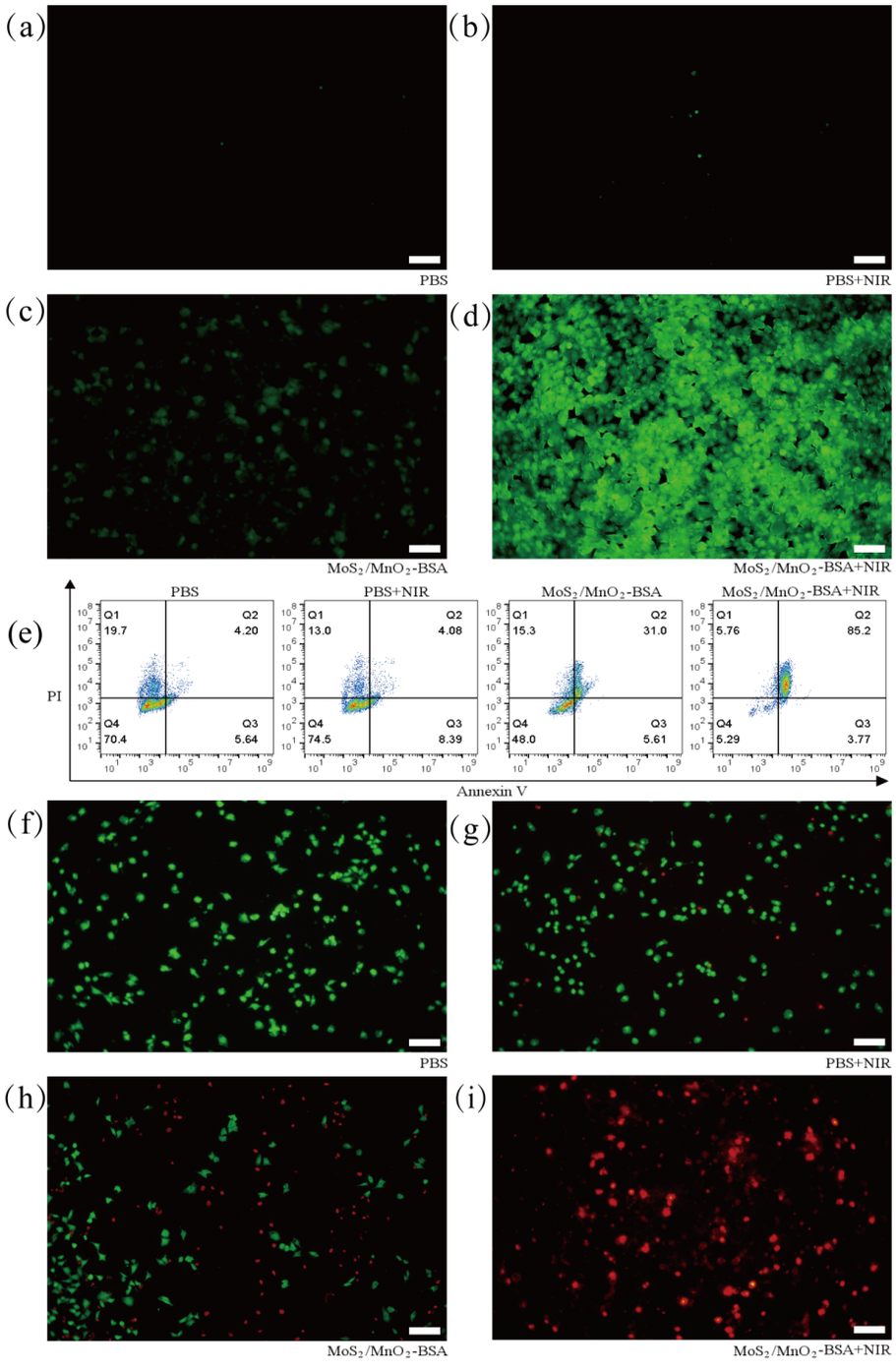

Fig. 4 (a–d) Fluorescence images of MGC-803 cells treated with DCFH-DA and MoS_2/MnO_2–BSA nanocomposites, with or without 808 nm (1.0 W·cm^{-2}) irradiation. **(e)** Apoptosis was analyzed by flow cytometry. **(f–i)** Calcein AM- and PI-stained MGC-803 cells exhibited fluorescence after different treatments: (Scale bar: 50 nm).

group. This finding implies that CDT combined with PT has a more potent synergistic effect on cancer cells in nanoplatforms than CDT alone.

In vitro therapeutic effect of MoS_2/MnO_2–BSA

PI and calcium xanthophyll AM staining were used to further illustrate the positive therapeutic effects of the MoS_2/MnO_2–BSA nanocomposites on MGC-803 cells. The MoS_2/MnO_2–BSA nanocomposite group displayed increased red luminescence, suggesting that •OH had damaged the MGC-803 cells. On the other hand, the laser and control groups displayed minimal colored fluorescence (dead cells) and green solid fluorescence (live cells) (Figs. 4(f) and 4(g)). After 10 min of 808 nm laser irradiation, more robust red fluorescence was observed (Fig. 4(i)), suggesting that the MoS_2/MnO_2–BSA nanocomposites made by the PTT-enhanced CDT had effective antitumor

properties. These results indicate that the MoS_2/MnO_2–BSA nanocomposites can effectively enhance the synergistic CDT/PTT effect.

Conclusions

We constructed a stable MoS_2/MnO_2–BSA nanomaterial for the combined •OH generation and optothermal cancer therapies. The biocompatible MoS_2/MnO_2–BSA nanoplatforms were built by modifying BSA onto MoS_2/MnO_2 nanomaterials. A simple and efficient sequential catalytic treatment approach was designed. First, the nanomaterial reacts with H_2O_2 in the TME to produce large amounts of toxic •OH. Second, under 808-nm laser irradiation, PTT-induced hyperthermia greatly enhanced the CDT effect of MoS_2/MnO_2–BSA and promoted the •OH generation efficiency. It displayed high cytotoxicity in the TME and realized the CDT-PTT synergistic impact [30].

Developing highly effective anticancer drugs remains a very promising and unmet need. The key to the prospect of anticancer medicines lies in their therapeutic efficacy, toxicity, and biocompatibility. MoS_2/MnO_2–BSA has a strong killing effect on cancer cells, and due to the excellent spatiotemporal selectivity of the 808 nm laser treatment, MoS_2/MnO_2–BSA can significantly avoid toxic side effects in cancer treatment. Additionally, Mo and Mn in MoS_2/MnO_2–BSA are essential trace elements for human survival. This work provides new insights into the development of more effective and safer nanocatalytic therapies for future clinical applications [31].

CRediT Author Statement

Lingle Zhang, **Xiaoqing Qian**, and **Kai Yang** designed and directed the study; **Lingle Zhang** and **Xiaoqing Qian** collected the data and wrote the paper; and the other authors helped with the statistical analysis. All the authors have read and approved the final manuscript.

Acknowledgements

This work was supported by the National Natural Scientific Fund (81971714).

Conflict of Interests

The authors declare that no competing interests exist.

Data Availability

The datasets used and zanalyzed during the current study are available from the corresponding author upon reasonable request.

References

[1] H. Lin, Y. Chen, J.L. Shi. Nanoparticle-triggered *in situ* catalytic chemical reactions for tumour-specific therapy. *Chemical Society Reviews*, 2018, 47(6): 1938−1958. https://doi.org/10.1039/C7CS00471K

[2] Y. Wang, K. Qi, S.S. Yu, et al. Revealing the intrinsic peroxidase-like catalytic mechanism of heterogeneous single-atom co-MoS_2. *Nano-Micro Letters*, 2019, 11(1): 102. https://doi.org/10.1007/s40820-019-0324-7

[3] C.D. Yang, M. Zhou, C. He, et al. Augmenting intrinsic fenton-like activities of MOF-derived catalysts via N-molecule-assisted self-catalyzed carbonization. *Nano-Micro Letters*, 2019, 11(1): 87. https://doi.org/10.1007/s40820-019-0319-4

[4] M.F. Huo, L.Y. Wang, Y. Chen, et al. Tumor-selective catalytic nanomedicine by nanocatalyst delivery. *Nature Communications*, 2017, 8(1): 357. https://doi.org/10.1038/s41467-017-00424-8

[5] W.Q. Wang, Y.L. Jin, Z.A. Xu, et al. Stimuli-activatable nanomedicines for chemodynamic therapy of cancer. *WIREs Nanomedicine and Nanobiotechnology*, 2020, 12(4): e1614. https://doi.org/10.1002/wnan.1614

[6] Z.X. Xie, S. Liang, X.C. Cai, et al. O_2-Cu/ZIF-8@Ce6/ZIF-8@F127 composite as a tumor microenvironment-responsive nanoplatform with enhanced photo-/chemodynamic antitumor efficacy. *ACS Applied Materials & Interfaces*, 2019, 11(35): 31671−31680. https://doi.org/10.1021/acsami.9b10685

[7] Y. Liu, W.Y. Zhen, L.H. Jin, et al. All-in-one theranostic nanoagent with enhanced reactive oxygen species generation and modulating tumor microenvironment ability for effective tumor eradication. *ACS Nano*, 2018, 12(5): 4886−4893. https://doi.org/10.1021/acsnano.8b01893

[8] S.S. Wan, Q. Cheng, X. Zeng, et al. A Mn(III)-sealed metal–organic framework nanosystem for redox-unlocked tumor theranostics. *ACS Nano*, 2019, 13(6): 6561−6571. https://doi.org/10.1021/acsnano.9b00300

[9] S.T. Gao, Y. Jin, K. Ge, et al. Self-supply of O_2 and H_2O_2 by a nanocatalytic medicine to enhance combined chemo/chemodynamic therapy. *Advanced Science*, 2019, 6(24): 1902137. https://doi.org/10.1002/advs.201902137

[10] Y.X. Liu, Q. Jia, Q.W. Guo, et al. Simultaneously activating highly selective ratiometric MRI and synergistic therapy in response to intratumoral oxidability and acidity. *Biomaterials*, 2018, 180: 104−116. https://doi.org/10.1016/j.biomaterials.2018.07.025

[11] L.-Y. Duan, Y.-J. Wang, J.-W. Liu, et al. Tumor-selective catalytic nanosystem for activatable theranostics. *Chemical Communications*, 2018, 54(59): 8214−8217. https://doi.org/10.1039/C8CC03922D

[12] J. Park, D.H. Lim, H.J. Lim, et al. Size dependent

macrophage responses and toxicological effects of Ag nanoparticles. *Chemical Communications*, 2011, 47(15): 4382−4384. https://doi.org/10.1039/C1CC10357A

[13] R.Z. Hu, Y. Fang, M.F. Huo, et al. Ultrasmall $Cu_{2-x}S$ nanodots as photothermal-enhanced Fenton nanocatalysts for synergistic tumor therapy at NIR-II biowindow. *Biomaterials*, 2019, 206: 101−114. https://doi.org/10.1016/j.biomaterials.2019.03.014

[14] Z. Wang, B. Liu, Q.Q. Sun, et al. Fusiform-like copper(II)-based metal–organic framework through relief hypoxia and GSH-depletion co-enhanced starvation and chemodynamic synergetic cancer therapy. *ACS Applied Materials & Interfaces*, 2020, 12(15): 17254−17267. https://doi.org/10.1021/acsami.0c01539

[15] S. Nandi, S.K. Bhunia, L.L. Zeiri, et al. Bifunctional carbon-dot-WS_2 nanorods for photothermal therapy and cell imaging. *Chemistry – A European Journal*, 2017, 23(4): 963−969. https://doi.org/10.1002/chem.201604787

[16] R.R. Deng, X.J. Xie, M. Vendrell, et al. Intracellular glutathione detection using MnO_2-nanosheet-modified upconversion nanoparticles. *Journal of the American Chemical Society*, 2011, 133(50): 20168−20171. https://doi.org/10.1021/ja2100774

[17] F.F. Cao, L. Zhang, H. Wang, et al. Defect-rich adhesive nanozymes as efficient antibiotics for enhanced bacterial inhibition. *Angewandte Chemie*, 2019, 58(45): 16236−16242. https://doi.org/10.1002/anie.201908289

[18] Z.Y. Wang, Y.M. Ju, Z. Ali, et al. Near-infrared light and tumor microenvironment dual responsive size-switchable nanocapsules for multimodal tumor theranostics. *Nature Communications*, 2019, 10(1): 4418. https://doi.org/10.1038/s41467-019-12142-4

[19] T. Liu, S.X. Shi, C. Liang, et al. Iron oxide decorated MoS_2 nanosheets with double PEGylation for chelator-free radiolabeling and multimodal imaging guided photothermal therapy. *ACS Nano*, 2015, 9(1): 950−960. https://doi.org/10.1021/nn506757x

[20] J. Yu, W.Y. Yin, X.P. Zheng, et al. Smart MoS_2/Fe_3O_4 nanotheranostic for magnetically targeted photothermal therapy guided by magnetic resonance/photoacoustic imaging. *Theranostics*, 2015, 5(9): 931−945. https://doi.org/10.7150/thno.11802

[21] S.S. Chou, B. Kaehr, J. Kim, et al. Chemically exfoliated MoS_2 as near-infrared photothermal agents. *Angewandte Chemie*, 2013, 52(15): 4160−4164. https://doi.org/10.1002/anie.201209229

[22] C.B. Liu, J.Q. Chen, Y. Zhu, et al. Highly sensitive MoS_2-indocyanine green hybrid for photoacoustic imaging of orthotopic brain glioma at deep site. *Nano-Micro Letters*, 2018, 10(3): 48. https://doi.org/10.1007/s40820-018-0202-8

[23] W.Y. Yin, J. Yu, F.T. Lv, et al. Functionalized nano-MoS_2 with peroxidase catalytic and near-infrared photothermal activities for safe and synergetic wound antibacterial applications. *ACS Nano*, 2016, 10(12): 11000−11011. https://doi.org/10.1021/acsnano.6b05810

[24] B.H. Tang, W.L. Li, Y.C. Chang, et al. A supramolecular radical dimer: High-efficiency NIR-II photothermal conversion and therapy. *Angewandte Chemie*, 2019, 58(43): 15526−15531. https://doi.org/10.1002/anie.201910257

[25] X.Z. Wu, Y.K. Suo, H. Shi, et al. Deep-tissue photothermal therapy using laser illumination at NIR-IIa window. *Nano-Micro Letters*, 2020, 12(1): 38. https://doi.org/10.1007/s40820-020-0378-6

[26] J.L. Chen, H. Zhang, X.Q. Huang, et al. Antiangiogenesis-combined photothermal therapy in the second near-infrared window at laser powers below the skin tolerance threshold. *Nano-Micro Letters*, 2019, 11(1): 93. https://doi.org/10.1007/s40820-019-0327-4

[27] W. Feng, X.G. Han, R.Y. Wang, et al. Nanocatalysts-augmented and photothermal-enhanced tumor-specific sequential nanocatalytic therapy in both NIR-I and NIR-II biowindows. *Advanced Materials*, 2019, 31(5): e1805919. https://doi.org/10.1002/adma.201805919

[28] S.T. Zhang, L.H. Jin, J.H. Liu, et al. Boosting chemodynamic therapy by the synergistic effect of co-catalyze and photothermal effect triggered by the second near-infrared light. *Nano-Micro Letters*, 2020, 12(1): 180. https://doi.org/10.1007/s40820-020-00516-z

[29] F. Jiang, B.B. Ding, S. Liang, et al. Intelligent MoS_2–CuO heterostructures with multiplexed imaging and remarkably enhanced antitumor efficacy via synergetic photothermal therapy/chemodynamic therapy/immunotherapy. *Biomaterials*, 2021, 268: 120545. https://doi.org/10.1016/j.biomaterials.2020.120545

[30] J.L. Jiang, X.Y. Cui, Y.X. Huang, et al. Advances and prospects in integrated nano-oncology. *Nano Biomedicine and Engineering*, 2024, 16(2): 152−187. https://doi.org/10.26599/nbe.2024.9290060

[31] R.S. Tade, M.P. More. Emerging application of graphene quantum dots in photodynamic/photothermal and hyperthermia therapies for cancer treatment. *Nano Biomedicine and Engineering*, 2024. https://doi.org/10.26599/nbe.2024.9290083

© The author(s) 2025. This is an open-access article distributed under the terms of the Creative Commons Attribution 4.0 International License (CC BY) (http://creativecommons.org/licenses/by/4.0/), which permits unrestricted use, distribution, and reproduction in any medium, provided the original author and source are credited.